A Laser-Induced Fluorescence Diagnostic for HERMeS and High-Power Electric Propulsion

65th JANNAF Propulsion Meeting/9th Spacecraft Propulsion Subcommittee
Long Beach, CA, May 21 – 24, 2017

Wensheng Huang, Hani Kamhawi, and Daniel A. Herman
National Aeronautics and Space Administration Glenn Research Center
Cleveland, OH

ABSTRACT

NASA is continuing the development of a 12.5-kW Hall thruster system, which is baselined in a phased exploration concept to expand human presence to cis-lunar space and eventually to Mars. The development team is transitioning knowledge gained from the testing of the government-built Technology Development Unit (TDU) to the contractor-built Engineering Development Unit (EDU). A new laser-induced fluorescence diagnostic that is compatible with the testing of engineering hardware was developed to obtain data for thruster model validation in the lowest background pressure achievable. Prior to performing the test on the EDU, the team performed a functional checkout test of this new diagnostic using the TDU. In addition to providing a checkout of the diagnostic, this test provided data that can be correlated to electron mobility for comparison to the EDU at a later date. A number of technical challenges related to large test facilities and interfacing with engineering hardware were overcome while implementing the new laser diagnostic system. The initial data set was in good agreement with prior optical and non-optical diagnostics data collected on the TDU thrusters. This data set also revealed the spatial origin of high angle ions that have been of concern for spacecraft integration.

ABBREVIATIONS

AEPS	=	Advanced Electric Propulsion System	JPL	=	Jet Propulsion Laboratory
CEX	=	Charge-exchange	LIF	=	Laser-Induced Fluorescence
EDU	=	Engineering Development Unit	RFC	=	Reference Firing Condition
GRC	=	Glenn Research Center	SEP	=	Solar Electric Propulsion
HEOMD	=	Human Exploration and Operations Mission Directorate	SNR	=	Signal-to-Noise Ratio
			STMD	=	Space Technology Mission Directorate
HERMeS	=	Hall Effect Rocket with Magnetic Shielding	TDM	=	Technology Demonstration Mission
			TDU	=	Technology Development Unit
IPS	=	Ion Propulsion System	VF	=	Vacuum Facility

INTRODUCTION

FOR missions beyond low Earth orbit, spacecraft size and mass can be dominated by onboard chemical propulsion systems and propellants that may constitute more than 50 percent of spacecraft mass. This impact can be substantially reduced through the utilization of Solar Electric Propulsion (SEP) due to its substantially higher specific impulse. Studies performed for NASA's Human Exploration and Operations Mission Directorate (HEOMD) and Science Mission Directorate have demonstrated that a 40 kW-class SEP capability can be enabling for both near term and future architectures and science missions.[1]

Since 2012 NASA has been developing a high power Hall thruster electric propulsion string that can serve as the building block for realizing a 40-kW-class SEP capability. NASA continues to evolve a human exploration approach to expand human presence beyond low-Earth orbit and to do so, where practical, in a manner involving international, academic, and industry partners.[2] NASA publicly presented

a phased exploration concept at the HEOMD Committee of the NASA Advisory Council meeting on March 28, 2017.[3] NASA presented an evolutionary human exploration architecture, called Lunar Orbital Platform – Gateway, to expand human presence deeper into the solar system through a phased approach including cis-lunar flight testing and validation of exploration capability before crewed missions beyond the Earth-Moon system and eventual crewed Mars missions. One of the key objectives is to achieve human exploration of Mars and beyond through the prioritization of those technologies and capabilities best suited for such a mission in accordance with the stepping stone approach to exploration.[4] High-power solar electric propulsion is one of those key technologies that has been prioritized because of its significant exploration benefits. A high-power, 40 kW-class Hall thruster propulsion system provides significant capability and represents, along with flexible blanket solar array technology, a readily scalable technology with a clear path to much higher power systems.

The Hall thruster system development, led by the NASA Glenn Research Center (GRC) and the Jet Propulsion Laboratory (JPL), began with the maturation of the 12.5-kW Hall thruster and power processing unit. The technology development work has transitioned to Aerojet Rocketdyne via a competitive procurement selection for the Advanced Electric Propulsion System (AEPS). The AEPS contract includes the development, qualification, and multiple flight electric propulsion string deliveries. The AEPS Electric Propulsion string consists of the Hall thruster, power processing unit (including digital control and interface functionality), xenon flow controller, and associated intra-string harnesses. These components are also collectively known as the Ion Propulsion System (IPS). NASA continues to support the AEPS development leveraging in-house expertise, plasma modeling capability, and world-class test facilities. NASA also executes AEPS and mission risk reduction activities to support the AEPS development and mission application.

Risk reduction activities are being carried out on the precursor to AEPS known as the Hall Effect Rocket with Magnetic Shielding (HERMeS).[6,7] The specifications for the 12.5-kW HERMeS are enhanced compared to the current state of the art.[6] Characteristics of the thruster include high system efficiency (≥57%), high specific impulse (up to 3000 s), and high propellant throughput capability (1770 kg). Additionally, HERMeS was designed to deliver similar system efficiency at a more modest specific impulse of 2000 seconds. High specific impulse operation supports mission concepts with high total-impulse requirements like deep-space exploration missions, while the modest specific impulse operation is beneficial for time-critical operations like LEO to GEO orbit raising.

A series of tests are being performed on three HERMeS Technology Development Units (TDUs).[7] Figure 2 shows a diagram of the testing on the HERMeS TDUs thus far as well as tests that are planned. Testing on the TDU1 included the propellant uniformity test,[8] magnetic shielding characterization test,[9] performance characterization test,[10-12] thermal characterization test,[13,14] facility effect characterization test,[10,12,15] and the first wear test campaign. The performance, thermal, and facility effect characterization tests were performed with a single test setup. The first wear test campaign, completed in 2016, included the electrical configuration characterization test,[16] two short duration tests,[17] and a long wear test.[17,18] TDU2 underwent an acceleration zone characterization test[19] and a pole erosion characterization test.[20] TDU2 will undergo the environmental test campaign. TDU3 was used in a second performance characterization test[21] and, together with TDU1, in a second wear test campaign.[22]

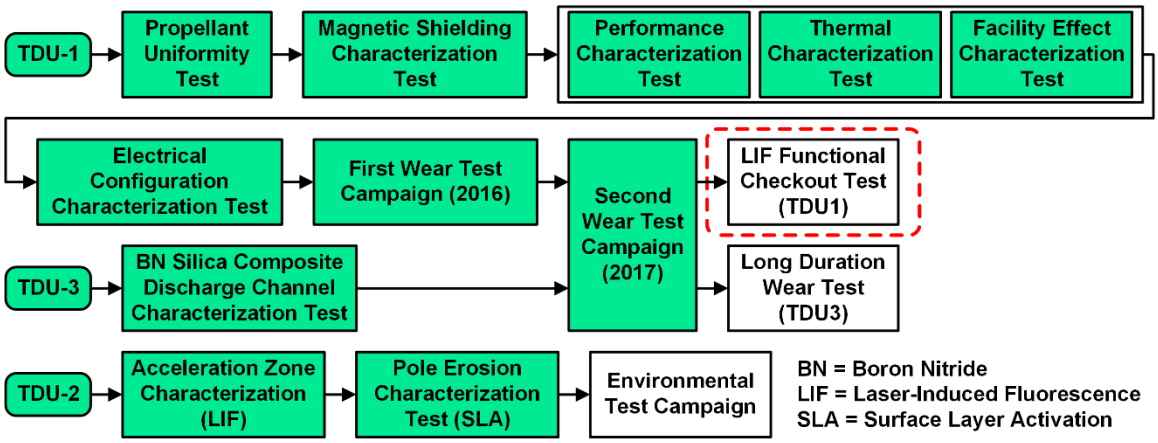

Figure 1. A diagram of the TDU test campaign.

Additionally, GRC Vacuum Facility 6 (VF6) was reconfigured to reconstitute high-power electric propulsion testing capability, which was followed by a series of verification and validation tests to confirm facility readiness.[23] VF6 was then used for parts of the second wear test campaign.[22]

During early risk reduction testing performed on the H6 Hall thruster, the plasma in the discharge channel was found to be strongly perturbed by the injection of physical probes into the discharge channel.[24] The team decided to instead rely on non-invasive laser-induced fluorescence (LIF) techniques to obtain the discharge channel plasma data needed for model validation. A key driver of Hall thruster plasma dynamics is the spatial distribution of electron mobility, also called the mobility profile. Laser-induced fluorescence (LIF) velocimetry can measure velocity distribution functions, which can be correlated to the mobility profile and provide an effective assessment of any differences between the plasma dynamics of the EDU and TDU.

NASA GRC has developed a new LIF diagnostic system that is fully compatible with the testing of high-power engineering electric propulsion devices. The new laser diagnostic system was functionally checked during a test using TDU1 in VF6. The system was then used to study various test conditions. Regions of interest in the obtained data set include the main acceleration zone, near-chamfer regions, and near the pole covers of the thruster. The data set also covered different discharge voltages, magnetic field strengths, and background pressure. Due to time constraints, only data for the 300 V and 600 V nominal operating condition is shown in this paper with additional data to be published in the future. This paper will begin by discussing the experimental setup and technical challenges associated with implementing LIF in a large vacuum facility that interfaces with engineering hardware. The paper will then discuss preliminary results from the LIF functional checkout test.

EXPERIMENTAL SETUP

To simplify plot labeling, throttle points are labeled as vvv-kk.k, where vvv is the discharge voltage in volts and kk.k is the discharge power in kilowatts.

Unless otherwise noted, all spatial positions around the thruster are normalized based on the region of interest. For the thruster discharge channel, spatial positions are normalized by the discharge channel width, where R = 0 is the inner wall, R = 1 is the outer wall, Z = 0 is the exit plane as defined by the inner front pole cover downstream surface, and Z is positive in the downstream direction.

THRUSTER AND TEST OPERATING CONDITIONS

All data presented in this work were collected with the HERMeS TDU1. The HERMeS TDU was designed to be a 12.5 kW, 3000 s, magnetically-shielded Hall thruster. The thruster had been operated over discharge voltages ranging from 300 to 800 V, corresponding to a specific impulse range of 2000 to

3000 s at full power. The thruster had also been throttled over discharge powers ranging from 0.6 to 12.5 kW.[10] The cathode mass flow rate was maintained at 7% of the anode mass flow rate.

Thruster magnet coils were energized so that the magnetic shielding topology was always maintained. The only degree of freedom in the magnetic field setting was the strength of the magnetic field. Peak radial magnetic field strength along the discharge channel centerline was chosen as the reference when referring to the strength of the magnetic field. A single magnetic field strength value was chosen as the nominal value for all operating conditions. This value was set to provide the highest thruster efficiency possible while maintaining margin against oscillation mode transitions. Figure 3 shows a picture of the NASA HERMeS TDU1 on the LIF test stand.

The specifications for the TDUs included seven Reference Firing Conditions (RFCs), which were throttle points that would be used in all TDU testing. Though the full operational range of the TDUs extends well beyond the RFCs, testing was constrained to the RFCs to limit testing cost. Table 1 lists the RFCs. The testing described in this paper focused on two of the RFCs, which are marked with asterisks.

For the testing described in this paper, the thruster body was isolated from the test stand and connected to the cathode. Prior testing had determined that this cathode-tied configuration was associated with low pole cover erosion and can be readily implemented in flight.[16,18]

Table 1. Table of Reference Firing Conditions.

Label	Discharge voltage, V	Discharge power, kW
300-2.7	**300**	**2.7**
***300-6.25**	**300**	**6.25**
400-8.3	**400**	**8.33**
500-10.4	**500**	**10.4**
500-12.5	**500**	**12.5**
***600-12.5**	**600**	**12.5**
700-12.5	**700**	**12.5**

*RFCs that were the focus of the testing described in this paper.

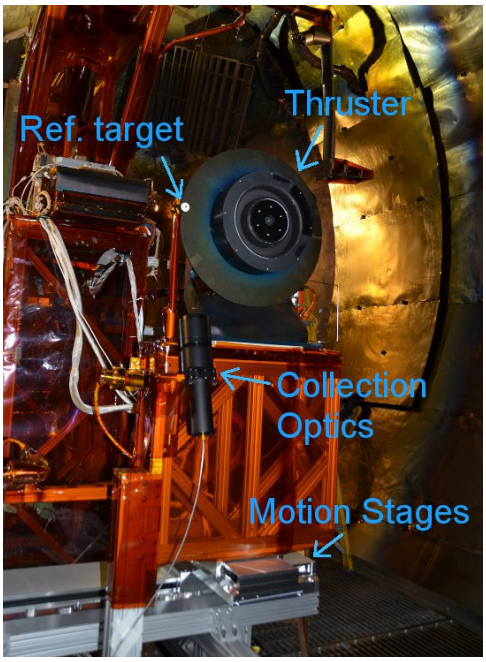

Figure 2. NASA HERMeS TDU1 and thrust stand setup.

TEST FACILITY

Testing was performed in Vacuum Facility 6 at NASA GRC. This cylindrical facility is 7.6 m in diameter, 21.3 m long, and was evacuated with a set of cryo-pumps. The thruster was mounted on a test stand that can be moved horizontally with two cross-mounted motion stages. Figure 3 shows the thruster mounted on the test stand. Also in the figure are the reference target used for laser alignment, the collection optics, and the motion stages that move the test stand.

Background pressure near the thruster was monitored with two ion gauges, which were calibrated on xenon against spinning rotor gauge. Gauge readings were corrected for temperature and direction relative to background flux via methods described in Yim and Burt.[25] Uncertainty in the calculated pressure was dominated by electrical and electronic noise, which was estimated by the manufacturer to be ±6% of the reading. The background pressure near the thruster for the two RFCs described in this paper was 1.2×10^{-5} Torr.

Research-grade xenon propellant was supplied via commercially available mass flow controllers to the thruster and cathode. These mass flow controllers were calibrated using research-grade xenon prior to testing. Typical uncertainty of measurement was ±1% of reading.

Electrical power was supplied to the thruster with commercially available power supplies. Separate power supplies supported the main discharge, cathode heater, keeper, inner magnet, and outer magnet. An electrical filter was placed between the thruster and the discharge power supply. All power supplies and the filter were located outside of the vacuum facility.

DIAGNOSTICS

The LIF velocimetry scheme used in the LIF functional checkout test in VF6 excites the XEII 834.953 nm (vac) transition and collects fluorescence from the 542.066 nm (vac) transition. This singly-charged xenon ion transition has an unusually narrow hyperfine structure that cannot be easily resolved even when probed with special techniques.[26] At the same time, the narrowness of the hyperfine structure means that associated broadening in the lineshape for data obtained in the accelerating plasma of a Hall thruster is at most 4-5%.[26] Figure 4 shows a diagram of the LIF scheme used.

Figure 5 shows the equipment used to inject laser light into the vacuum facility. The laser was a taper-amplified diode laser that output up to 500 mW at 835 nm. Wavelength was monitored via a Fizeau-type wavemeter and an optogalvanic cell. The laser beam entering the optogalvanic cell was mechanically chopped at ~1.6 kHz. The laser beam was also monitored with photodiode to track the variation in laser power. The laser beam was split into three branches. Each branch passed through a separate electro-optical modulator and was collimated into optical fibers. A modulation frequency study showed that the signal-to-noise ratio (SNR) optimized at around 300 kHz to 350 kHz in modulation frequency.

Figure 6 shows a diagram of the optics setup inside the vacuum facility. Three sets of injection optics where deployed. The optical fibers from the air-side setup were sent to each of the three sets of injection optics. Each set of injection optics had two motors that allowed remote control of the tilt and pan. The optics on axis 1, the axial axis, was protected from most of the heat of the plasma by a shield. The

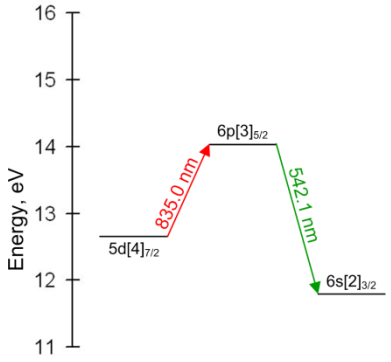

Figure 3. Transition diagram for Xe II LIF at 834.953 nm (vac).

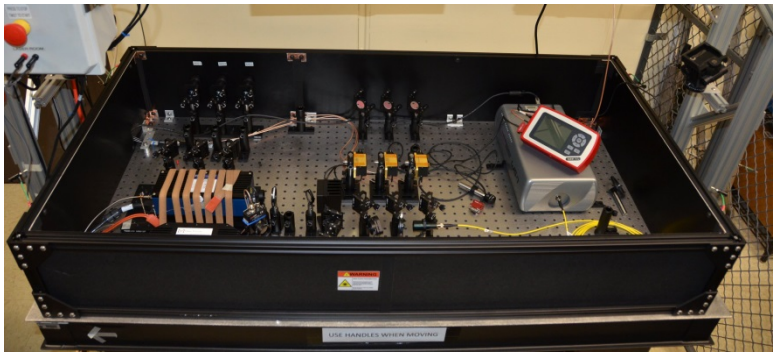

Figure 4. Air-side laser injection setup.

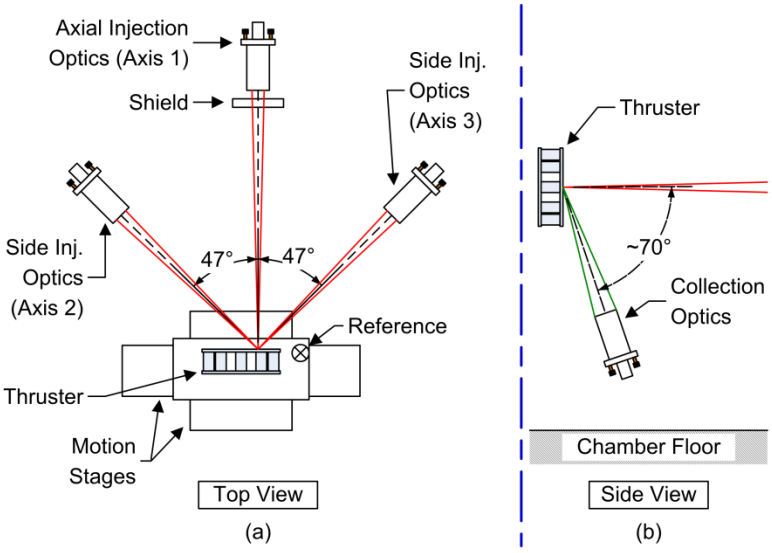

Figure 5. Vacuum-side optical setup.

Figure 6. Fluorescence signal processing equipment.

thruster was mounted to the motion stages that provide radial and axial movements. A reference target was mounted at a known distance from the thruster in the same plane as the three injected laser beams. Two cameras monitored the positions of the injected laser beams relative to the reference target. The collection optics were mounted 70° out of the laser plane. An optical fiber carried fluorescence signal from the collection optics out of the vacuum facility.

Figure 7 shows a picture of the equipment that processed the fluorescence signal. The light from the collection optical fiber was collimated into a monochromator and sent to a photomultiplier. The photomultiplier current was converted to voltage via a high-speed trans-impedance amplifier. The output voltage signal was coupled into three digital lock-in amplifiers. A fourth digital lock-in amplifier measures the signal from the optogalvanic cell. A computer controls the movement of various stages, sweeps the laser wavelength, and records the various output signals.

TECHNICAL CHALLENGES

MAINTAINING LASER ALIGNMENT

Shifts in laser alignment is typically driven by the length of various support structure holding the optics and the amount of heating of the structure during thruster operation. Higher power electric propulsion testing requires a larger test facility to manage facility interaction effects and apply greater heat load on optics in the plume. Maintaining laser alignment becomes more difficult as the power level of the test article increases.

The LIF system described in this paper relies on an improved version of a previous alignment approach that was proven on a 6-kW Hall thruster in a large test facility.[27] The new LIF system made two key improvements over the previous approach. Previously, laser light from the injection optics were focused on to a reference pin and scattered light collected by the collection optics. This setup was extremely sensitive to the relative position of the laser beam, pin, and the collection optics making the pin a very effective alignment tool. However, if the laser beam ever drifted too far out of position (over one mm), recovering the alignment without venting was often impossible. The new LIF system incorporates a washer coated with white ceramic paste and two in-vacuum cameras to help identify the relative position of the laser beams with respect to the reference pin. Furthermore, laser light striking the pin produces unique scattering patterns that were easy to recognize and provided an additional feedback beyond the scatter light collected by the collection optics for fine alignment. Figure 8 shows a close-up image of the reference target. Figure 9 shows an image captured by an in-vacuum camera during an alignment check while the thruster was operating. The in-vacuum cameras had their IR-cut filters removed.

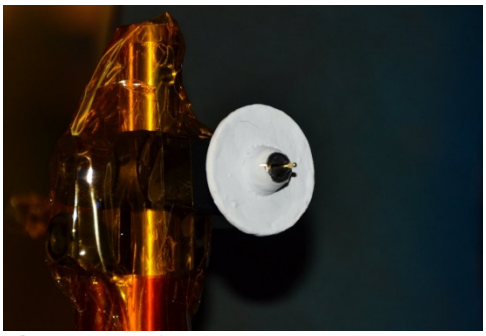

Figure 7. Reference target.

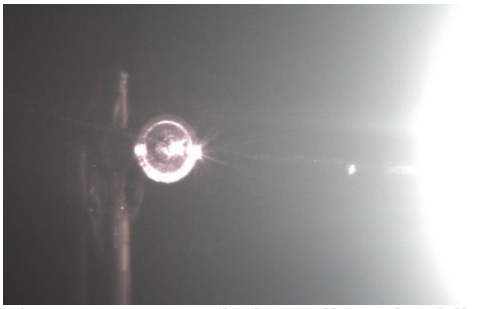

Figure 8. Laser being aligned while thruster operated.

The second improvement to help maintain laser alignment was made to the axial injection optics support structure. A copper tube was sandwiched inside of the support structure to create a cooling loop. A chiller maintains the temperature of the coolant. Although the shield between the thruster and the axial injection optics absorbs the majority of the heat coming from the thruster plasma, the shield radiated and conducted some of the heat to its surrounding. Some of the radiated emission from the thruster also passed through the transparent window in the shield that the laser passed through. The use of active cooling enabled data acquisition periods of several hours between alignment adjustments that lasted several minutes. Figure 10 shows the shield and axial injection optics support during thruster operation. Thruster plume appears to have a green tint because the photograph was taken through a green-tinted window, which was a laser safety window.

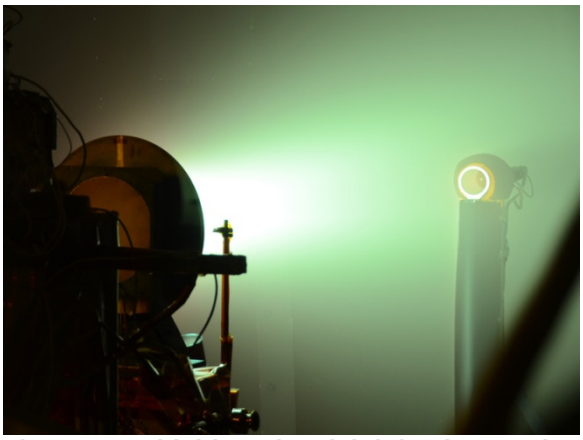

Figure 9. Shield and axial injection optics support illuminated by thruster light.

BAKE-ABLE FLEXIBLE PROPELLANT DELIVERY

Another technical challenge when developing the LIF system was the delivery of propellant to the thruster on a moving test stand. In the past, synthetic rubber tubing was used for propellant delivery. However, propellant purity levels required by EDU hardware can typically only be met by baked out metal tubing. A straight metal tube was not sufficiently flexible to accommodate the range of motion that the test stand underwent. A new arrangement of metal tubing made of three sets of coils was used to allow baking of the tubing and provide the necessary flexibility for motion of the test stand.

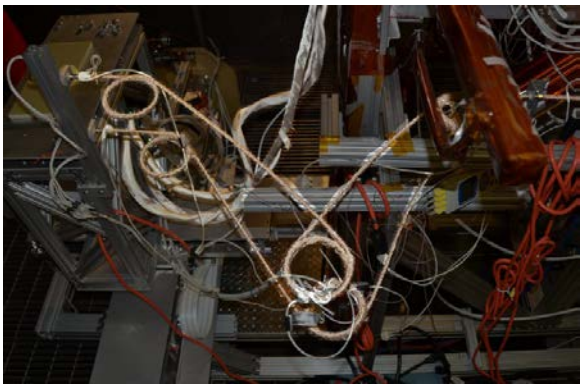

Figure 10. The propellant line metal tubing coils wrapped in heat tapes for bakeout.

Figure 11 show a photograph of the metal tubing coils wrapped in heat tapes for bakeout. The coils on the two propellant lines were wound slightly differently to study the different characteristics. They were made of stainless steel tubing bent at three locations into coils, which form rotating joints. The middle joint had more turns than the other two joints because the middle joint bent the most. The metal tubing coils were fully baked and leak checked and performed well during testing.

DATA ANALYSIS

ANALYSIS METHOD

A saturation study was performed at the beginning of the test campaign to pick out injection laser power that balances saturation broadening and SNR (i.e. high laser intensity leads to higher SNR but also more saturation broadening). The amount of broadening was kept to below 10%. A more in-depth analysis will be perform later to determine the amount of broadening for each scan. For the data presented in this paper, the amount of saturation broadening is no more than 10%.

No attempt was made to remove the hyperfine structure broadening as they contribute no more than 5% broadening.[26] Since lineshape broadening add as square root of the sum of squares of individual broadening terms, hyperfine structure broadening may be overshadowed by saturation broadening.

Treatment hyperfine structure broadening is saved for when in-depth saturation broadening analysis are performed.

The first step in the data analysis was to convert readings from the wavemeter and optogalvanic cell into frequency shift from the stationary transition frequency. This frequency shift was sometimes referred to as the detuning. The detuning was then converted into a velocity scale.

The intensity data was corrected for changes in laser power by using a combination of photodiode and thermopile measurements. First, the laser power as measured by the thermopile and the photodiode were collected in a control study. Then, the photodiode measure during data acquisition was corrected by the results of the control study to provide an accurate measurement of the laser power. This correction removed artificial features that may have been created in the intensity data due to variations in laser power as the wavelength varied. For the intensity data presented in this paper, no smoothing was performed on the velocity distribution functions (VDFs).

In theory, entire VDFs can be averaged to obtain the mean velocity. In practice, randomness in the noise translates into uncertainty in the mean velocity if the entire VDF was used to generate the mean. Instead, averaging was performed by first finding where the signal drops to half of maximum and only the data in between were used. This is referred to as threshold-based averaging with a 50% threshold. A lower percentage threshold yields a more accurate average until the threshold meets the noise. A high percentage threshold turns the average into most probable velocity. 50% strikes balance across the entire data set to be presented and caused the analysis program to ignore low lying populations like tails on VDFs. More advanced data analysis methods will be attempted in the future.

UNCERTAINTY ANALYSIS

The uncertainty in position was dominated by drift in alignment of the optics. The alignment procedure used in this LIF test rejects data where alignment drifted by more than 0.5 mm from the reference.

The SNR was an important metric in assessing uncertainty in the data. The SNR was defined as the ratio of the peak signal divided by the standard deviation of the noise. Typically, any trace with an SNR of 3 or less was considered to be statistically insignificant. At this value of SNR, any peak present was barely detectable against the noise.

The uncertainty in the mean velocity was dominated by the amount of noise present. The uncertainty from the wavemeter and optogalvanic cell combination was ±50 m/s and much lower than the uncertainty from the noise. Scanning resolution limits the absolute accuracy of the mean velocity to approximately ±100 m/s. Where SNR was high, the total uncertainty was close to this ±100 m/s limit but where SNR was low (just high enough to make out the presence of the peak), the uncertainty could reach ±1000 m/s. In-depth uncertainty analysis will be performed in the future to quantify the uncertainty for each data point.

RESULTS AND DISCUSSION

PRELIMINARY RESULTS

Figure 12 shows the axial velocity distributions found along the discharge channel centerline for the 300 V, 6.25 kW condition. Figure 13 shows the same for the 600 V, 12.5 kW condition. Data in these figures were collected from axis 1.

From Figure 12, one could see that the ion VDF broadened as the ions accelerated before narrowing again. The broadening of ion VDFs inside the acceleration zone had been tied to axial movement in the accelerating potential profile associated with breathing mode oscillation.[27,28]

From Figure 13, one could see a different sort of VDF broadening that was likely associated with a sinusoidal oscillation unique to magnetically-shielded Hall thruster. More precisely, this oscillation mode has only been observed to dominate for magnetically-shielded Hall thrusters operating at high discharge voltage (500+ V).[11] As the ions were accelerated, their VDFs began to exhibit two-peak structures that were highly reminiscent of probability density function of harmonic oscillators (see Figure 2 of Huang, et al.[27] for an example of how harmonic oscillation give rise to probability density function with two peaks). Notably, the largest separation between the two peaks was associated with the highest change in velocity. This behavior agrees well with the idea that the acceleration profile was moving axially as a whole. Looking at it from a different perspective, if the accelerating profile underwent the same amount of axial movement everywhere, the location with the highest potential gradient would also display the highest variation in potential.

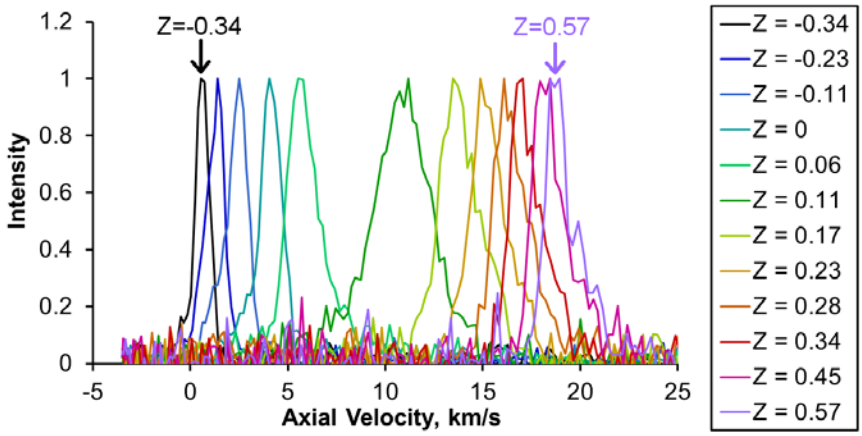

Figure 11. VDFs at select locations along the discharge channel centerline for the 300 V, 6.25 kW condition.

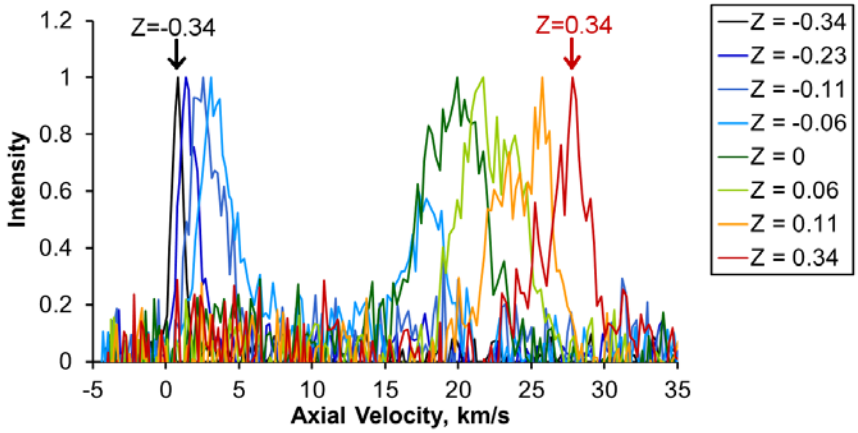

Figure 12. VDFs at select locations along the discharge channel centerline for the 600 V, 12.5 kW condition.

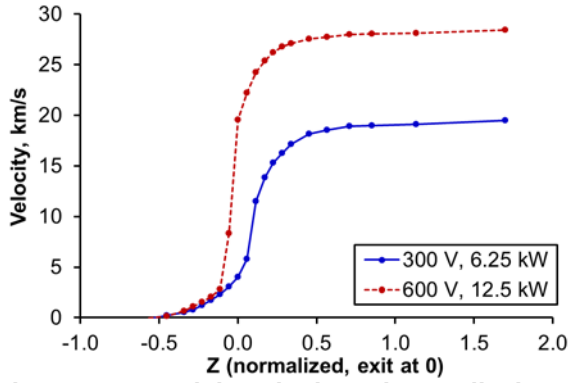

Figure 13. Axial velocity along discharge channel centerline of TDU1.

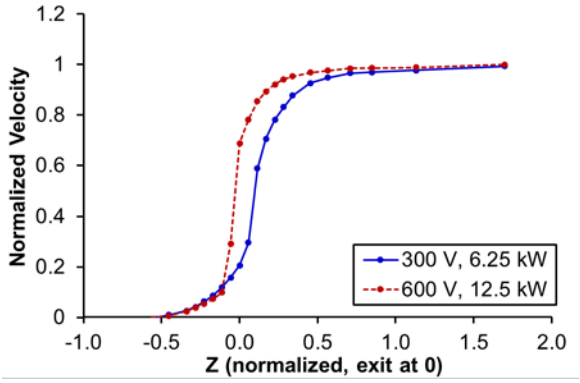

Figure 14. Normalized axial velocity along discharge channel centerline of TDU1.

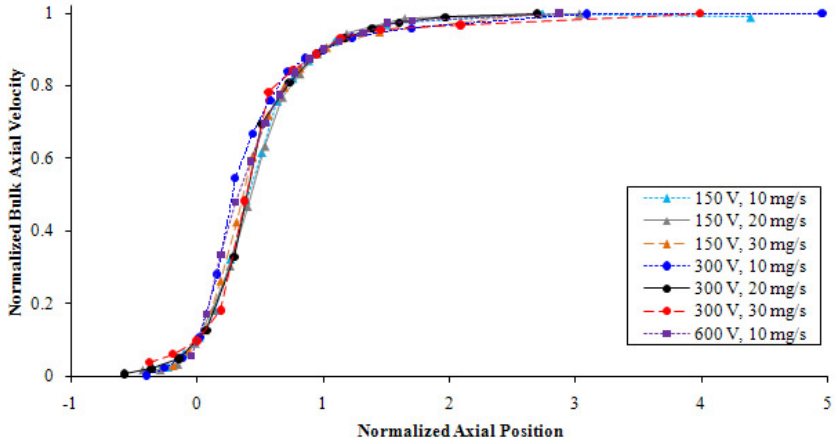

Figure 15. Normalized axial velocity along discharge channel centerline of the H6 Hall thruster.[27]

Figure 14 shows the threshold-based averaged axial velocity as a function of position for the 300 V, 6.25 kW and 600 V, 12.5 kW operating conditions. This data is in very good agreement with another LIF study performed on TDU2 by Chaplin, et al.[19]. The TDU2 study was performed in the Owens chamber at JPL. Ion gauges were installed at matching distances and orientations for the LIF studies conducted at JPL and GRC and measured background pressures were within 10% of each other.

Figure 15 shows the threshold-based averaged axial velocity normalized by the maximum velocity for each condition. Notably, the acceleration profile was sharper and more upstream for the 600 V, 12.5 kW operating condition than for the 300 V, 6.25 kW operating condition. The sharpest rise in velocity for the 600 V, 12.5 kW data corresponded to the two-peak VDFs shown in Figure 13. This behavior contrasts with the H6 6-kW Hall thruster, which does not utilize magnetic shielding. From Figure 13 of Huang, et al.[27], reproduced here as Figure 16, the H6 exhibited a nearly uniform acceleration profile when similarly normalized. The difference in behavior between the TDU and the H6 was not likely to be due to power levels as both thrusters operated at similar power densities. The most likely reason for the difference in behavior was the difference in magnetic field topology though further investigation is needed.

Figures 17 and 18 show the vector plot obtained from utilizing the 2D LIF data for the 300 V, 6.25 kW and 600 V, 12.5 kW conditions, respectively. Data on axes 2 and 3 generally had higher SNR than data on axis 1 and was used to generate the vector plots. Lower SNR on axis 1 was due in part to the fact that the VDFs tended to be more spread out in the direction of travel so a mostly axial ion population tended to have a broader VDF with a lower peak height along the axial direction than along any other directions. Recall that SNR was defined as peak height divided by standard deviation of the noise. Quantification of the differences in axial velocity measured by axis 1 laser beam versus calculated from axes 2 and 3 can be found in the appendix.

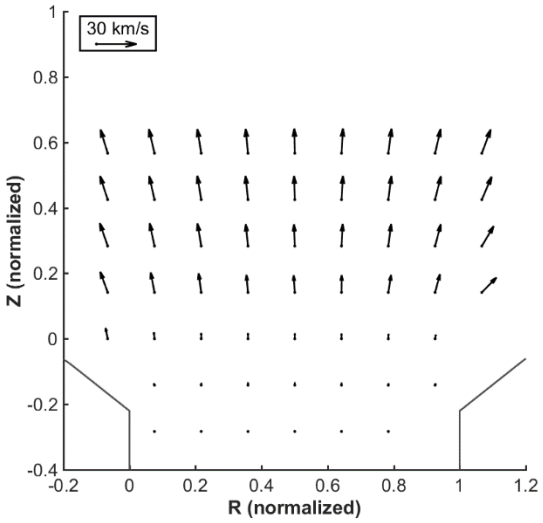

Figure 16. Averaged velocity vector in and near the discharge channel for the 300 V, 6.25 kW condition.

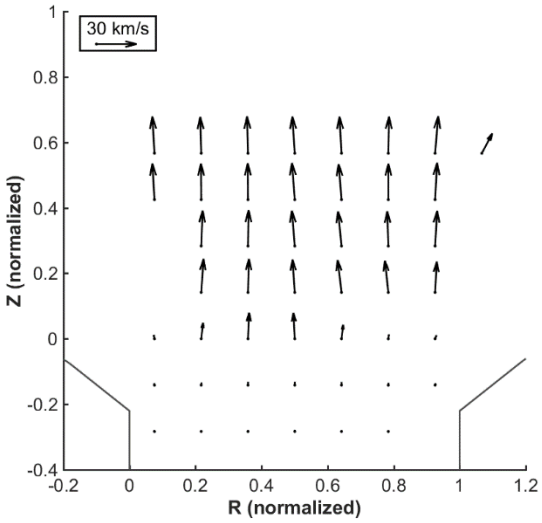

Figure 17. Averaged velocity vector in and near the discharge channel for the 600 V, 12.5 kW condition.

From Figures 17 and 18, one can see that the ion beam was noticeable more collimated for the 600 V, 12.5 kW condition than for the 300 V, 6.25 kW condition. This behavior is in agreement with past Faraday probe measurements on the TDUs.[18] Notably, the ions have picked up a fair bit of energy by the time they reached the exit plane (Z = 0) for the 600 V, 12.5 kW condition but not for the 300 V, 6.25 kW condition, as was shown in Figure 14.

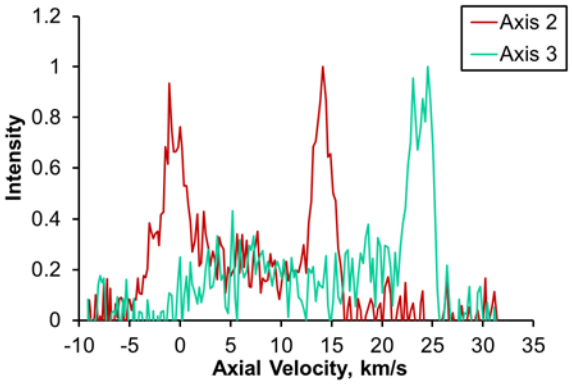

Figure 18. Axis 2 and 3 VDFs at the top right most vector location in Figure 18.

Interestingly, one of the vector (top right most) in the 600 V, 12.5 kW condition looks out of family with the rest. Close inspection of the VDF revealed the presence of two peaks in the VDFs. Figure 19 shows the axes 2 and 3 VDFs at this location for the 600 V, 12.5 kW condition. Assuming the high energy peak on each axis is associated with each other, further analysis of these VDFs show that the high energy peak was in family with the rest of the vectors in Figure 18. In contrast, the low energy peak was pointed much more in the radial direction. An extended study was performed in this region at 600 V, 12.5 kW to further illuminate the situation.

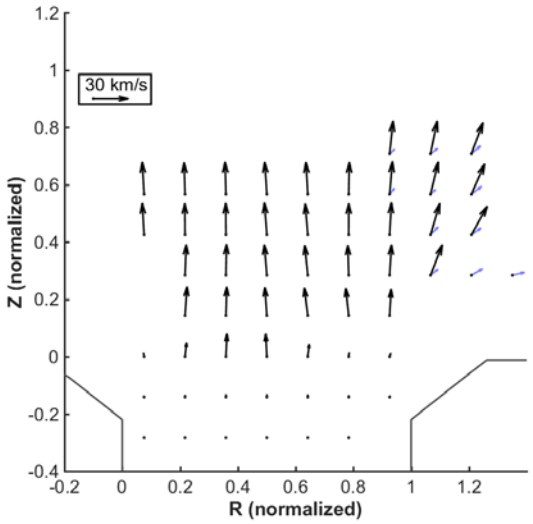

Figure 19. Averaged velocity vector in and near the discharge channel for the 600 V, 12.5 kW condition with expanded location matrix.

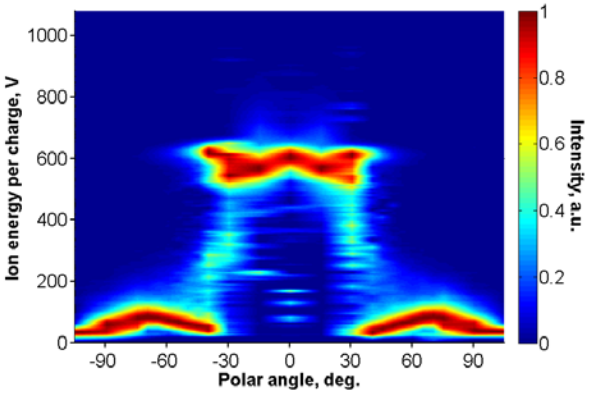

Figure 20. Ion energy per charge versus polar angle for the 600 V, 12.5 kW condition.[18]

EXTENDED STUDY

Figure 20 shows the vector plot for the 600 V, 12.5 kW condition with expanded location matrix and in-depth analysis that individually identify the two peaks present at each location. The higher energy arrow was colored black and the low energy arrow was colored blue. This figure illustrates how the low energy population moved away from the discharge channel at a much greater angle from the firing axis than the high energy population. Average energy of the low energy population at the outermost radial positions was about 80 eV, with high energy tails that reached beyond 200 eV. Average energies of the low energy population at the more inner radial positions were as low as 20 eV.

Figure 21 shows a plot of ion energy per charge versus polar angle for the 600 V, 12.5 kW condition obtained via retarding potential analyzer measurements.[18] The dark red areas show which ion energy population was dominant at that polar angle. Specifically, the high energy ions were dominant inside of ±40° with respect to the firing axis while the low energy ions were dominant outside of those angles. Figure 20 appears to be in excellent agreement with Figure 21 as the high energy ions (black arrows) were generally within ±40° of the firing axis while the low energy ions (blue arrows) were much more divergent. The energies of the low energy ions were also seen to reach beyond 200 eV at some angles in Figure 21. The extended LIF study appears to have captured some portion of the creation and subsequent acceleration of low energy ions that eventually form the wings of the far-field plasma plume. One candidate for explaining the presence of these low energy ions is charge exchange collisions. Further analysis and modeling is needed to confirm this possibility.

If the low energy population moving away from the thruster at high angles were indeed charge exchange ions then they should also have been present for the 300 V, 6.25 kW condition. And examination of the VDFs collected at the rightmost locations (R = 1.07) for the 300 V, 6.25 kW condition showed that there were indeed a low energy population present. Figure 22 shows the VDFs at R = 1.07, Z = 0.28 for the 300 V, 6.25 kW condition. Unlike the VDFs found in the same region for the 600 V, 12.5 kW condition, the low energy population does not show up as strongly relative to the high energy population for the 300 V, 6.25 kW condition. This is likely due to the fact that the high energy population was more divergent for the 300 V, 6.25 kW condition and was dominant over the low energy population over a larger range of angles. Figure 23 shows a plot of ion energy per charge versus polar angle for the 300 V, 6.25 kW condition.[18] This figure confirms that the high energy ions were dominant over a large range of angles (±80°). If the low energy population was indeed charge-exchange ions, their presence

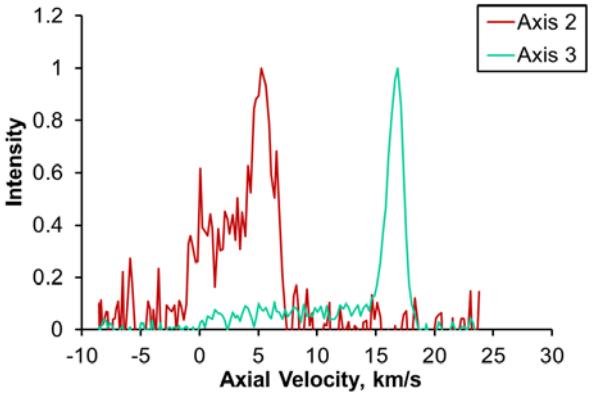

Figure 21. Axis 2 and 3 VDFs at R = 1.07 and Z = 0.28 for the 300 V, 6.25 kW condition.

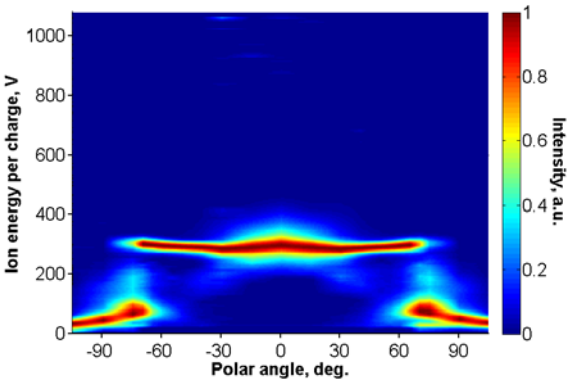

Figure 22. Ion energy per charge versus polar angle for the 300 V, 6.25 kW condition.[18]

would not be a surprise as the plasma density in the near-field was more than sufficient to generate these ions. What was unexpected was the apparent acceleration (beyond 200 eV for some ions) that this low energy population undergoes as they travel away from the high energy population. Note that the possibility also exists that some of the low energy population were ions that were ionized well downstream of the main ionization zone. However, in this region just downstream of the bulk of the Hall current, charge-exchange collision frequencies are much higher than ionization collision frequencies.

An alternate hypothesis to the charge-exchange ion idea is the possibility that the low energy population was a result of plasma oscillations (like the breathing mode for 300 V operation and the harmonic oscillator mode for 600 V operation[11]). A close inspection of the axis 2 VDF in Figure 19 reveals that this VDF looked very similar to the Z = -0.06 VDF in Figure 13. There is a possibility, that like the Z = -0.06 VDF on the discharge channel centerline, the VDFs along the radially outer region of the discharge channel that display two peaks were actually displaying the time-averaged result of oscillating VDFs. The counter argument against this hypothesis include that there is no clear mechanism for discharge channel oscillations to generate this level of ion energy variation so far outside of the discharge channel. Time-resolved LIF could be used to determine which of the two hypotheses is correct.

SUMMARY AND CONCLUSIONS

NASA GRC has developed a new LIF diagnostic system for use with high-power electric propulsion devices. The use of this LIF system was successfully demonstrated in a test in VF6 with the HERMeS TDU. Initial test results at 300 V, 6.25 kW and 600 V, 12.5 kW were in excellent agreement with another TDU test in JPL's Owens chamber when the two tests were conducted at the same background pressure.[19] An extended spatial map of the plasma plume demonstrated that the new system was able to detect low energy ions that may consist mostly of charge-exchange ions. These low energy ions were found at axial locations downstream of the main ionization zone and were found to undergo some amount of acceleration as they travel at a high angle relatively the firing axis away from the high energy ions. An examination of far-field retarding potential analyzer data showed good correlation between the trajectories and energies of the low and high energy populations found in the near-field and their angular positions in the far-field. Further analysis and modeling activities should provide positive identification of the ions found at high angles in the thruster plume that are of greatest concern for spacecraft integration.

APPENDIX

Equations for calculating the averaged axial and radial velocities for the setup illustrated in Figure 6 will be derived in this appendix. When planning an LIF setup that uses only two injection axes, one should ideally be orthogonal to the other to minimize uncertainty associated with velocity vector projection. However, a realistic setup cannot always achieve perfect orthogonality. The equations will be derived with arbitrary angles between the axial axis and the injection axes. Figure 24 shows a diagram of the associated setup. Let θ_2 be the angle between axes 2 and the axial axis, and let θ_3 be the same between axis 3 and the axial axis. V_2 and V_3, the averaged velocities along axes 2 and 3, respectively, can be calculated by geometry from the V_z, the averaged axial velocity, and V_r, the averaged radial velocity as follows in Eqs. (1) and (2).

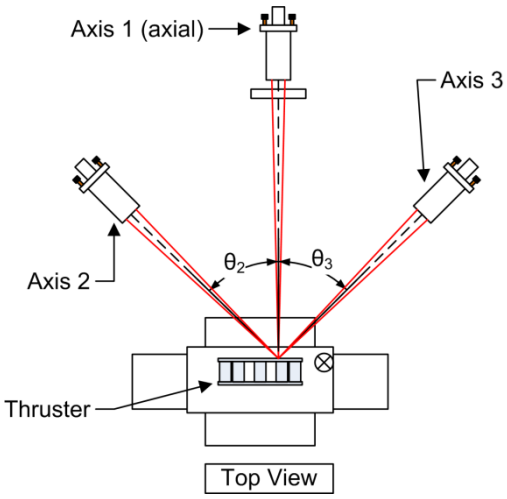

Figure 23. LIF setup with arbitrary axes 2 and 3 angles.

$$V_2 = V_z \cos\theta_2 - V_r \sin\theta_2 \quad (1)$$

$$V_3 = V_z \cos\theta_3 + V_r \sin\theta_3 \quad (2)$$

Solving for V_z and V_r yields Eqs. (3) and (4).

$$V_z = \frac{V_2 \sin\theta_3 + V_3 \sin\theta_2}{\cos\theta_2 \sin\theta_3 + \cos\theta_3 \sin\theta_2} \quad (3)$$

$$V_r = \frac{V_3 \cos\theta_2 - V_2 \cos\theta_3}{\cos\theta_2 \sin\theta_3 + \cos\theta_3 \sin\theta_2} \quad (4)$$

If $\theta_2 = \theta_3 = \theta$, Eqs. (3) and (4) can be simplified into Eqs. (5) and (6), respectively.

$$V_z = \frac{V_2 + V_3}{2\cos\theta} \quad (5)$$

$$V_r = \frac{V_3 - V_2}{2\sin\theta} \quad (6)$$

Eq.(5) was validated using data along the discharge channel of the TDU. Examination of data from both 300 V, 6.25 kW and 600 V, 12.5 kW shows that the discrepancy in average axial velocity was less than 2% when the averaged axial velocity was above 5 km/s and less than 5% between 1.5 and 5 km/s. For averaged axial velocities below 1.5 km/s (basically ions that have undergone negligible acceleration), the discrepancy in velocity was less than 150 m/s, which was a large number when expressed in percentage but was in fact only slightly larger than the measurement uncertainty of the LIF system. The use of threshold-based averaging instead of regular averaging was likely a contributor to the discrepancies though the alternative would have been accepting greater uncertainties in the averages from the inclusion of a greater amount of noise.

ACKNOWLEDGMENTS

The authors would like to thank the Space Technology Mission Directorate through the Solar Electric Propulsion Technology Demonstration Mission Project for funding the joint NASA GRC and JPL development of the HERMeS thruster and this work. The authors would like to thank Todd Tofil for managing the electric propulsion work within the SEP Project and the thruster lead, Richard R. Hofer, for managing the thruster work. The authors would also like to thank Li C. Chang, Maria Choi, Lauren K. Clayman, Jason Frieman, Timothy Gray, Christopher M. Griffiths, Thomas W. Haag, Jonathan A. Mackey, James L. Myers, Peter Peterson, Dale A. Robinson, Timothy R. Sarver-Verhey, and John T. Yim of the

NASA Glenn Research Center and Vernon H. Chaplin, Ryan W. Conversano, Ioannis G. Mikellides, Alejandro Lopez Ortega, and James E. Polk of the Jet Propulsion Laboratory for work on the SEP TDM HERMeS Hall thruster. And the authors would like to thank Luke Sorrelle, Michael McVetta, Derek Patterson, Kevin L. Blake, George P. Jacynycz, and Thomas A. Ralys for assembly of the test setup, and operation of the vacuum facility.

REFERENCES

1. Smith, B. K., Nazario, M. L., and Cunningham, C. C., ***Solar Electric Propulsion Vehicle Demonstration to Support Future Space Exploration Missions***, Space Propulsion 2012, Bordeaux, France, May 7-10, 2012.
2. Congress, ***National Aeronautics and Space Administration Transition Authorization Act of 2017***, 2017.
3. ***NASA's Journey to Mars***. 2015 [cited; Available from: http://www.nasa.gov/sites/default/files/atoms/files/journey-to-mars-next-steps-20151008_508.pdf.
4. Gerstenmaier, W. ***Progress in Defining the Deep Space Gateway and Transport Plan***. NASA Advisory Council Human Exploration and Operations Committee Meeting 2017 [cited; Available from: https://www.nasa.gov/sites/default/files/atoms/files/nss_chart_v23.pdf.
5. Manzella, D. and Hack, K., ***High-Power Solar Electric Propulsion for Future NASA Missions***, 50th AIAA/ASME/SAE/ASEE Joint Propulsion Conference, AIAA-2014-3718, doi:10.2514/6.2014-3718, Cleveland, OH, Jul 28-30, 2014.
6. Herman, D., et al., ***Overview of the Development and Mission Application of the Advanced Electric Propulsion System (AEPS)***, 35th International Electric Propulsion Conference, 2017-284, Atlanta, GA, Oct 8-12, 2017.
7. Hofer, R. R. and Kamhawi, H., ***Development Status of a 12.5 kW Hall Thruster for the Asteroid Redirect Robotic Mission***, 35th International Electric Propulsion Conference, 2017-231, Atlanta, GA, Oct 8-12, 2017.
8. Huang, W., Yim, J. T., and Kamhawi, H., ***Design and Empirical Assessment of the HERMeS Hall Thruster Propellant Manifold***, 62nd Joint Army-Navy-NASA-Air Force Propulsion Meeting, JANNAF-2015-3926, Nashville, TN, Jun 1-4, 2015.
9. Shastry, R., Huang, W., and Kamhawi, H., ***Near-Surface Plasma Characterization of the 12.5-kW NASA TDU1 Hall Thruster***, 51st AIAA/ASME/SAE/ASEE Joint Propulsion Conference, AIAA-2015-3919, doi:10.2514/6.2015-3919, Orlando, FL, Jul 27-29, 2015.
10. Kamhawi, H., et al., ***Performance and Facility Background Pressure Characterization Tests of NASA's 12.5-kW Hall Effect Rocket with Magnetic Shielding Thruster***, 34th International Electric Propulsion Conference, 2015-007, Kobe, Japan, Jul 4-10, 2015.
11. Huang, W., Kamhawi, H., and Haag, T. W., ***Plasma Oscillation Characterization of NASA's HERMeS Hall Thruster via High Speed Imaging***, 52nd AIAA/ASME/SAE/ASEE Joint Propulsion Conference, AIAA-2016-4829, doi:10.2514/6.2016-4829, Salt Lake City, UT, Jul 25-27, 2016.
12. Kamhawi, H., et al., ***Performance, Facility Pressure Effects, and Stability Characterization Tests of NASA's Hall Effect Rocket with Magnetic Shielding Thruster***, 52nd AIAA/ASME/SAE/ASEE Joint Propulsion Conference, AIAA-2016-4826, doi:10.2514/6.2016-4826, Salt Lake City, UT, Jul 25-27, 2016.
13. Huang, W., Kamhawi, H., Myers, J. L., Yim, J. T., and Neff, G., ***Non-Contact Thermal Characterization of NASA's HERMeS Hall Thruster***, 51st AIAA/ASME/SAE/ASEE Joint Propulsion Conference, AIAA-2015-3920, doi:10.2514/6.2015-3920, Orlando, FL, Jul 27-29, 2015.
14. Myers, J. L., Kamhawi, H., Yim, J. T., and Clayman, L., ***Hall Thruster Thermal Modeling and Test Data Correlation***, 52nd AIAA/ASME/SAE/ASEE Joint Propulsion Conference, AIAA-2016-4535, doi:10.2514/6.2016-4535, Salt Lake City, UT, Jul 25-27, 2016.
15. Huang, W., Kamhawi, H., Haag, T. W., Lopez Ortega, A., and Mikellides, I. G., ***Facility Effect Characterization Test of NASA's HERMeS Hall Thruster***, 52nd AIAA/ASME/SAE/ASEE Joint Propulsion Conference, AIAA-2016-4828, doi:10.2514/6.2016-4828, Salt Lake City, UT, Jul 25-27, 2016.
16. Peterson, P. Y., et al., ***NASA's HERMeS Hall Thruster Electrical Configuration Characterization*** 52nd AIAA/ASME/SAE/ASEE Joint Propulsion Conference, AIAA-2016-5027, doi:10.2514/6.2016-5027, Salt Lake City, UT, Jul 25-27, 2016.
17. Williams, G. J., et al., ***Wear Testing of the HERMeS Thruster***, 52nd AIAA/ASME/SAE/ASEE Joint Propulsion Conference, AIAA-2016-5025, doi:10.2514/6.2016-5025, Salt Lake City, UT, Jul 25-27, 2016.
18. Huang, W., et al., ***Plasma Plume Characterization of the HERMeS during a 1722-hr Wear Test Campaign***, 35th International Electric Propulsion Conference, 2017-307, Atlanta, GA, Oct 8-12, 2017.

19. Chaplin, V. H., et al., ***Laser Induced Fluorescence Measurements of the Acceleration Zone in the 12.5 kW HERMeS Hall Thruster***, 35th International Electric Propulsion Conference, 2017-229, Atlanta, GA, Oct 8-12, 2017.
20. Polk, J. E., et al., ***Inner Front Pole Erosion in the 12.5 kW HERMeS Hall Thruster Over a Range of Operating Conditions***, 35th International Electric Propulsion Conference, 2017-409, Atlanta, GA, Oct 8-12, 2017.
21. Kamhawi, H., et al., ***Performance and Stability Characterization of the HERMeS Thruster with M26 Boron Nitride Discharge Channel***, 35th International Electric Propulsion Conference, 2017-392, Atlanta, GA, Oct 8-12, 2017.
22. Williams, G. J., et al., ***Wear Trends of the HERMeS Thruster as a Function of Throttle Point***, 35th International Electric Propulsion Conference, 2017-207, Atlanta, GA, Oct 8-12, 2017.
23. Peterson, P. Y., et al., ***NASA Glenn Research Center Vacuum Facility 6 Reconfiguration for HERMeS and AEPS Programs***, 35th International Electric Propulsion Conference, 2017-028, Atlanta, GA, Oct 8-12, 2017.
24. Jorns, B. A., Goebel, D. M., and Hofer, R. R., ***Plasma Perturbations in High-Speed Probing of Hall Thruster Discharge Chambers: Quantification and Mitigation***, 51st AIAA/ASME/SAE/ASEE Joint Propulsion Conference, AIAA-2015-4006, doi:10.2514/6.2015-4006, Orlando, FL, Jul 27-29, 2015.
25. Yim, J. T. and Burt, J. M., ***Characterization of Vacuum Facility Background Gas Through Simulation and Considerations for Electric Propulsion Ground Testing***, 51st AIAA/ASME/SAE/ASEE Joint Propulsion Conference, AIAA-2015-3825, doi:10.2514/6.2015-3825, Orlando, FL, Jul 27-29, 2015.
26. Huang, W., Smith, T. B., and Gallimore, A. D., ***Obtaining Velocity Distribution using a Xenon Ion Line with Unknown Hyperfine Constants***, 40th AIAA Plasmadynamics and Laser Conference, AIAA-2009-4226, doi:10.2514/6.2009-4226, San Antonio, Texas, Jun 22-25, 2009.
27. Huang, W., Drenkow, B., and Gallimore, A. D., ***Laser-Induced Fluorescence of Singly-Charged Xenon Inside a 6-kW Hall Thruster***, 45th AIAA/ASME/SAE/ASEE Joint Propulsion Conference & Exhibit, AIAA-2009-5355, doi:10.2514/6.2009-5355, Denver, CO, Aug 2-5, 2009.
28. Durot, C. J., Georgin, M. P., and Gallimore, A. D., ***Time-Resolved Laser-Induced Fluorescence Measurements in the Plume of a 6-kW Hall Thruster***, 34th International Electric Propulsion Conference, 2015-399, Kobe, Japan, Jul 4-10, 2015.